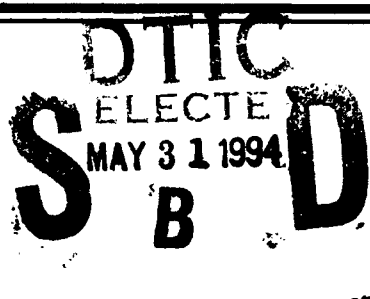


Naval Research Laboratory

Washington, DC 20375-5320



AD-A279 823



NRL/MR/6720--94-7472

PRS Scoping Study II: ZPIMP Predictions for Radiation Yields on a JUPITER-Class Generator

J. L. GIULIANI, Jr.
J. ROGERSON
J. DAVIS

*Radiation Hydrodynamic Branch
Plasmas Physics Division*

May 31, 1994

3786

94-16082



Approved for public release; distribution unlimited.

94 5 27 034

DTIC 94-16082-1

REPORT DOCUMENTATION PAGE			Form Approved OMB No. 0704-0188	
<small>Public reporting burden for this collection of information is estimated to average 1 hour per response, including the time for reviewing instructions, searching existing data sources, gathering and maintaining the data needed, and completing and reviewing the collection of information. Send comments regarding this burden estimate or any other aspect of this collection of information, including suggestions for reducing this burden, to Washington Headquarters Services, Directorate for Information Operations and Reports, 1215 Jefferson Davis Highway, Suite 1204, Arlington, VA 22202-4302, and to the Office of Management and Budget, Paperwork Reduction Project (0704-0188), Washington, DC 20503.</small>				
1. AGENCY USE ONLY (Leave Blank)		2. REPORT DATE May 31, 1994		3. REPORT TYPE AND DATES COVERED
4. TITLE AND SUBTITLE PRS Scoping Study II: ZPIMP Predictions for Radiation Yields on a JUPITER-Class Generator				5. FUNDING NUMBERS
6. AUTHOR(S) J.L. Giuliani, Jr., J. Rogerson, and J. Davis				
7. PERFORMING ORGANIZATION NAME(S) AND ADDRESS(ES) Naval Research Laboratory Washington, DC 20375-5320				8. PERFORMING ORGANIZATION REPORT NUMBER NRL/MR/6720-94-7472
9. SPONSORING/MONITORING AGENCY NAME(S) AND ADDRESS(ES) Defense Nuclear Agency RAEV Alexandria, VA 22310				10. SPONSORING/MONITORING AGENCY REPORT NUMBER
11. SUPPLEMENTARY NOTES				
12a. DISTRIBUTION/AVAILABILITY STATEMENT Approved for public release; distribution unlimited.				12b. DISTRIBUTION CODE
13. ABSTRACT (Maximum 200 words) A limited radiation-magnetohydrodynamics simulation code, ZPIMP, is used to predict radiation yields in various energy bins on a JUPITER-class machine. Elements of the simulation code are reviewed and calculations are made to compare the code with experimental K-shell yields from aluminum z-pinch on the SATURN generator. For a chosen viscosity parameter the simulated yields agree remarkably with the data. The same code is applied on an early version of the linear inductive voltage adder, but the projected krypton yields are disappointing. By increasing the compression through a lower viscosity parameter, the subsequent yields are significantly improved for weak implosions, showing that such a case is highly sensitive to the details of the dynamics. The capabilities of a ~60 MA JUPITER-class generator are surveyed with the ZPIMP code and the results for argon, krypton, and xenon are compared against the anticipated required source yields in five energy bins ranging from 0 to 60 keV. In the lowest bins (0-1 and 1-5 keV) JUPITER is well suited to reach the required yields, but in the highest bins (15-30 and 30-60 keV) the present calculations indicate that improvements in load design, understanding, and control are necessary to meet the requirements. Limitations of the ZPIMP calculations and directions for improving the PRS estimates for JUPITER are derived from the present work.				
14. SUBJECT TERMS Z-pinch Radiation hydrodynamics Plasma radiation sources				15. NUMBER OF PAGES 38
				16. PRICE CODE
17. SECURITY CLASSIFICATION OF REPORT UNCLASSIFIED		18. SECURITY CLASSIFICATION OF THIS PAGE UNCLASSIFIED		19. SECURITY CLASSIFICATION OF ABSTRACT UNCLASSIFIED
				20. LIMITATION OF ABSTRACT UL

CONTENTS

I. Introduction	1
II. The ZPIMP Simulation Code	3
III. Comparison of ZPIMP Calculations with SATURN A2 Data	8
IV. Krypton Radiation Yields on a JUPITER-Class Generator	12
V. JUPITER Capabilities vs. Radiation Requirements	22
VI. Summary and Conclusions	27
Acknowledgments	31
References	32

PRS SCOPING STUDY II: ZPIMP PREDICTIONS FOR RADIATION YIELDS ON A JUPITER-CLASS GENERATOR

I. Introduction

The Defense Nuclear Agency (DNA) has long supported plasma radiation-source (PRS) development for assessing radiation hardening of various defense and communication systems. Existing pulsed power generators such as DOUBLE EAGLE, BLACKJACK 5, PHOENIX, and SATURN deliver from 3 to 10 MA of current to an imploding z pinch and can produce 25 – 75 kJ of Al K-shell radiation (≥ 1.6 keV photons) [Ref.1]. The DECADE generator under construction is designed to deliver ~ 20 MA of current to the front end. With a z-pinch load, DECADE is predicted to produce ~ 300 kJ of argon K-shell emission (≥ 3.1 keV photons) [Ref.2]. With the cessation of underground testing the next generation pulsed power driver will be required to produce mega-joules of radiation in the 0 – 15 keV range, and several hundred kilo-joules between 30 and 60 keV. The JUPITER Design Option Study Team (JDOST) was formed in the summer of 1993 to develop circuit models for this next generation machine. It is anticipated that the JUPITER machine will provide ~ 60 MA peak load current. In order to determine the potential radiation yields from such a machine, DNA has chartered the Plasma Physics Division at the Naval Research Laboratory to undertake a PRS scoping study. This is one of several papers reporting on the results and conclusions of that study.

In the precursor paper [Ref.3] to this report the Whitney-Thornhill scaling law [Refs.4 and 5] was generalized to account for two problems characteristic of imploding loads on super high current generators: (i) large initial radii, and (ii) weak implosions which barely thermalize high atomic number material like Kr into the K-shell ionization stage. The resultant algebraic relations for the radiation yield, termed the J-scaling law, depend on simple properties of the implosion: atomic number Z , mass loading M , pinch length ℓ , final kinetic energy E_K , and stagnation radius R_f . The overriding utility of the scaling approach lies in the rapid and efficient investigation of large ranges in load and machine parameter space. Reference 3 used the J-scaling law in conjunction with circuit models to estimate yields on the two leading design candidates for JUPITER: the Linear Inductive voltage Adder (LIA) and the Inductive Energy Store (IES) designs. The peak yields for the standard point designs of both machines were found to range from ~ 7 MJ for Ar, through ~ 3 MJ for Kr, to ~ 0.3 MJ for Xe. Furthermore, the J-scaling law was used to survey the Ar, Kr, and Xe yield dependence on pinch length, front end inductance, and switch behavior for various modifications of the standard designs.

The ease of application of the J-scaling law belies the large investment in its development. The precursor to the J-scaling law was based on and tested against Al experiments on existing machines [Refs.4]. In this regime one finds good agreement with the data [Ref.1]. However, Ref.3 noted serious issues in extending the K-shell scaling law to JUPITER load configurations. First,

it is highly unclear whether the Z scaling, derived for low atomic number elements, applies to the *ionization dynamics* of krypton and xenon, where the L- and M-shell states can act as a major energy sink. Second, the *stagnation physics* at ~ 60 MA on JUPITER may present significant differences from the case at ~ 10 MA, where the scaling was tested. Third, the optimized yields on JUPITER are found at large radii but the effects of *instabilities, asymmetries, and turbulence* are unknown in this regime.

The goal of the present report is to improve upon the scaling law yield estimates by addressing in more detail the first two issues: ionization and stagnation physics. A simple 1-D simulation code, ZPIMP, will be employed to follow the z pinch dynamics on a JUPITER-class generator through implosion, thermalization, and subsequent bounce, while coupled to an atomic physics and radiation transport model. This will provide an improved assessment of the PRS capabilities on JUPITER, lead to a better understanding of the unique stagnation physics at super high currents, and, because of the capability of spectral resolution in a full radiation calculation, allow a direct comparison with stated radiation requirements in various energy bins. It should not be presumed that scaling law calculations are irrelevant in the face of more complex modeling. As will be pointed out throughout this paper, scaling law estimates will be used to examine the gross dependence of the yield in the load mass – initial radius plane. This allows the ZPIMP studies to focus on a selected region of parameter space with a limited set of runs to determine the optimal conditions. As the ZPIMP code provides minimal spatial resolution by treating the plasma shell as a single zone, it too will need to be replaced with more complex multi-zone and 2-D simulations. One should view the scaling law followed by the ZPIMP calculations as the beginning in a sequence of steps leading to more refined, complex, and more time consuming, yield estimates.

Section II contains an overview of the components in the ZPIMP (Z-Pinch IMplosion) simulation code. The equations describing the dynamics of the plasma shell as a single zone are summarized along with the magnetic induction equation, the lumped circuit model driving the pinch, the atomic physics models, and the radiation transport technique. A low mass core zone inside the plasma shell is also modeled. Since the code takes a Lagrangian viewpoint, an artificial viscosity, q_{vis} , is defined to effectively soften the implosion [Ref.5]. In Section III a value for q_{vis} is determined by matching the K-shell yield from a large set of SATURN aluminum experiments. The resultant code is then used to investigate krypton implosions on a JUPITER-class generator in Section IV. The JUPITER model in the present paper is a Thevenin equivalent circuit of an early LIA design. For the q_{vis} appropriate to SATURN, JUPITER promises poor yields in the higher photon energy bins. To enhance the yields the pinch compression at stagnation is increased by arbitrarily lowering q_{vis} . Section V presents a list of radiation fluence test requirements in various energy bins for JUPITER and converts them to source yields subject to uniformity criteria and

debris standoff distances. Using ZPIMP with the above mentioned adder circuit, a search over load mass and initial radius is performed to optimize yields from Ar, Kr, and Xe. The resulting capabilities from low and high compression pinches are then compared with the required source yields in tabular form. The results in the moderate to high energy (≥ 5 keV) photon range point to a fundamental task for load physics on JUPITER: the need to achieve \gtrsim tenfold compression in initial to final pinch radius. The last Section (VI) contains a summary of the present findings, limitations on the conclusions, and proposed directions for continued research on JUPITER loads.

II. The ZPIMP Simulation Code

ZPIMP is a cylindrically symmetric, 1-D, radiation-magnetohydrodynamic simulation code for modeling z-pinch implosions with a lumped circuit model for the generator. The simplifying feature of the ZPIMP code is the treatment of the main plasma load as a single zone lying between an inner radius R_i and an outer radius R_o . This zone carries a mean ion (electron) density $n_i(n_e)$, a mean ion (electron) temperature $T_i(T_e)$, a mean ionization level $\langle Z \rangle = n_e/n_i$, and a specific ionization/excitation internal energy ϵ_{ions} . Figure 1 shows the plasma nomenclature and the geometric variables. The dynamic equations are found by volume integration of the standard momentum and energy equations. Details of the formulation can be found in Ref.6. Only a summary of the model equations are presented here. The separate momentum equations for the inner and outer radii are, respectively,

$$\frac{d}{dt} \left(\frac{3}{4} \frac{M}{\ell} v_o \right) = (p_i + p_e) 2\pi R_o + q_{vis,s} 2\pi R_s - \frac{1}{c} \int_{R_i}^{R_o} J_z B_\phi 2\pi r dr, \quad (1)$$

and

$$\frac{d}{dt} \left(\frac{1}{4} \frac{M}{\ell} v_i \right) = -(p_i + p_e - p_c) 2\pi R_i - (q_{vis,s} 2\pi R_s - q_{vis,c} \pi R_i) - \frac{1}{c} \int_0^{R_i} J_z B_\phi 2\pi r dr. \quad (2)$$

Here M is the total shell mass; ℓ the pinch length; $v_o(v_i)$ the velocity of the outer (inner) radius; p_i the ion shell pressure $= n_i k_B T_i$ (k_B is Boltzmann's constant); p_e the electron shell pressure $= n_e k_B T_e$; p_c a core pressure for the region between the axis and R_i ; J_z the axial current density; and B_ϕ the azimuthal magnetic field. R_s is the midpoint of the plasma shell. Because the finite differencing is essentially Lagrangian, both the plasma shell (subscript s) and the core region (subscript c) have a tensor artificial viscosity [Ref.7] of the form

$$q_{vis} = \beta_{vis} \rho \Delta v \left(\frac{1}{2} \Delta v + \frac{1}{2} C_{sp} \right), \quad (3)$$

where β_{vis} is the non-dimensional viscosity parameter, ρ is the mass density of the zone, Δv is the velocity difference between the interfaces of the zone, and C_{sp} is the zone's sound speed $= \sqrt{5/3(p/\rho)}$. If the zone is expanding, q_{vis} is set to zero. The parameter β_{vis} is adjusted in the next section to obtain overall agreement with SATURN aluminum data.

The equations for the ion and electron internal energies in the plasma shell are given by

$$\frac{d}{dt} \left(\frac{M}{\ell} \epsilon_i \right) = -p_i 2\pi (R_o v_o - R_i v_i) - q_{vis,i} 2\pi R_o (v_o - v_i) + Q_{ie} \pi (R_o^2 - R_i^2), \quad (4)$$

and

$$\frac{d}{dt} \left(\langle Z \rangle \frac{m_e}{m_i} \frac{M}{\ell} \epsilon_e \right) = -p_e 2\pi (R_o v_o - R_i v_i) - Q_{ie} \pi (R_o^2 - R_i^2) + \int_0^{R_o} \eta J_z^2 2\pi r dr - \frac{\Lambda_{rad}}{\ell}. \quad (5)$$

The transport coefficients for the ion-electron thermal equilibration rate Q_{ie} and the resistivity η are taken from Braginskii [Ref.8]. The next to last term in eqn.(5) is the resistive heating rate in the shell, and Λ_{rad} is the plasma's radiation emission rate. An ideal gas law is assumed and the specific ionization/excitation energy ϵ_{ions} is part of the electron internal energy:

$$\epsilon_i = \frac{3}{2} k_B T_i / m_i; \quad (6a)$$

$$\epsilon_e = \frac{3}{2} k_B T_e / m_e + \epsilon_{ions}. \quad (6b)$$

The core region inside R_i is assigned 1% of the shell mass, has the same initial temperature as the shell, and is treated as a radiationless gas. Its energy equation

$$\frac{d}{dt} \left(\frac{3}{2} \pi R_i^2 p_c \right) = -p_c 2\pi R_i v_i - q_{vis,c} \pi R_i v_i, \quad (7)$$

reflects both compressional and viscous heating. The initial ZPIMP code described in Ref.6 did not include a core zone. Imaging diagnostics on a Russian aluminum wire experiment [Ref.9] indicate the formation of a hot core just prior to plasma assembly on axis. Detailed multi-zone radiation-magnetohydrodynamic simulations of argon implosions on DOUBLE EAGLE [Ref.10] used a low density inner core plasma in matching the spectral data for the mean density and temperature at stagnation. The importance of this dynamic feature was evidenced early in our present research by the failure to match ZPIMP calculations without a core to SATURN aluminum data presented in the next section. Hence the present ZPIMP version includes a simple, but adequate, treatment in eqn.(7) of the hot core formation in order to better reflect the observed stagnation physics.

The current density and magnetic field are related through Ampere's law

$$J_z = \frac{c}{4\pi} \frac{1}{r} \frac{\partial}{\partial r} (r B_\phi). \quad (8)$$

The magnetic field obeys an induction equation formed by combining a generalized Ohm's law with Faraday's law:

$$\frac{\partial B_\phi}{\partial t} + \frac{\partial}{\partial r}(v B_\phi) = \frac{\partial}{\partial r}(c\eta J_z). \quad (9)$$

In ZPIMP these field quantities can be calculated on a fine grid and then Maxwell stresses and the resistive heating are integrated over different volumes as shown in eqns.(1), (2), and (5).

The ionization dynamics and radiation transport is time split from the magnetohydrodynamics, i.e., the specific ionization/excitation energy ϵ_{ions} , the mean charge state $\langle Z \rangle$, and the radiation emission rate Λ_{rad} in the plasma shell zone are held constant during a hydro timestep. At the end of a hydro timestep and before the next one, the above three quantities are updated, subject to the conservation of total electron internal energy (6b).

Z-pinch implosions with four different elements will be considered: aluminum, argon, krypton, and xenon. For the first three of these materials the atomic level structure is defined through Detailed Configuration Accounting (DCA). For aluminum, the bare nucleus, all ground state levels and 121 excited levels spread through the upper eleven ionization stages are followed. Free-bound transitions to and from all of these levels are possible and 269 bound-bound transitions are considered. The numbers for argon are: stripped + eighteen ground states + 108 excited levels in the upper eleven stages, and 389 bound-bound transitions; and for krypton: stripped + thirty-six ground states + 61 excited levels in the upper eleven stages, and 184 bound-bound transitions. For each separate material the level populations are determined by a set of atomic rate equations

$$\frac{\partial f_{ki}}{\partial t} = \sum_j (\mathcal{R}_{jki} f_{ji} - \mathcal{R}_{kji} f_{ki}), \quad (10)$$

where f_{ki} is the fractional population of level k in the i 'th ionic species, and \mathcal{R}_{jki} is the net rate describing the transition in the i 'th species from the initial level j to the final level k . The net rate includes collisional ionization, excitation, and de-excitation, 3-body and radiative recombination, photo-ionization, pumping, radiative decay, and inner-shell absorption. In general the time derivative is neglected so that collisional-radiative equilibrium is achieved. Details on the solution techniques and rate coefficients are summarized in Duston, et al. [Ref.11].

For xenon, the detailed configuration accounting is a potential future development. Instead, an Average Atom (AA) approach is used wherein electrons take on non-integral occupation numbers within a screened hydrogenic model for the atomic structure. Our AA model includes 31 levels: all quantum sublevels n, ℓ from $n = 1$ to 7, and lumped sublevels for $n = 8, 9, 10$. Thirty-one recombination edges and 199 dipole allowed transitions are possible with this AA level structure. The formulas for the n, ℓ electronic energy level structure are taken from Perrot [Refs.12 and 13],

with the screening constants from More [Ref.14] and Marchand, et al. [Ref.15]. The atomic rates which couple different levels as in eqn.(10) and the radiative transition probabilities are based on the hydrogenic approximation of Post, et al. [Ref.16]. The present AA model has been under development for several years and represents a significant improvement over the standard model with only ten lumped levels.

Radiation emission from the plasma and opacity are dependent upon the local atomic-level populations, for not only are photons created by radiative recombination and decay transitions, such photons also lead to population redistribution. Thus the ionization dynamics and radiation transport is a strongly coupled problem and must be solved together. The radiation transport of the bound-bound and bound-free transitions are carried out using the probability-of-escape formalism described in Apruzese [Refs.17 and 18]. Multi-frequency transport is performed for the free-free radiation. Because the transport takes place across only one zone, the AA method for ionization dynamics can use a similar radiation routine as the DCA method.

The generator driving the plasma load is modeled in ZPIMP with a lumped circuit. For the circuits in this paper the machine is described by an open circuit voltage pulse V_{oc} , an impedance Z_o , and a front end inductance L_o . From the circuit viewpoint, the load consists of a variable inductance pinch of radius R_o and length ℓ surrounded by return current posts at R_w :

$$L_o \frac{dI}{dt} + Z_o I = V_{oc} - \frac{d}{dt} \left[\frac{2\ell}{c^2} \ln \left(\frac{R_w}{R_o} \right) I \right]. \quad (11)$$

In cgs units with $\mu_o = 4\pi/c^2$, where c is the speed of light, the vacuum magnetic field B is related to the load current through $B = 2I/rc$. The initial load inductance is given by

$$L_w = \frac{2\ell}{c^2} \ln \left(\frac{R_w}{R_o(t=0)} \right). \quad (12)$$

The generator is coupled implicitly to the plasma dynamics [eqn.(1)] and the field diffusion equation [eqn.(9)]. The magnetic and total plasma energy in the load region agrees with the time integrated power delivered to the load from eqn.(11) to better than 1%.

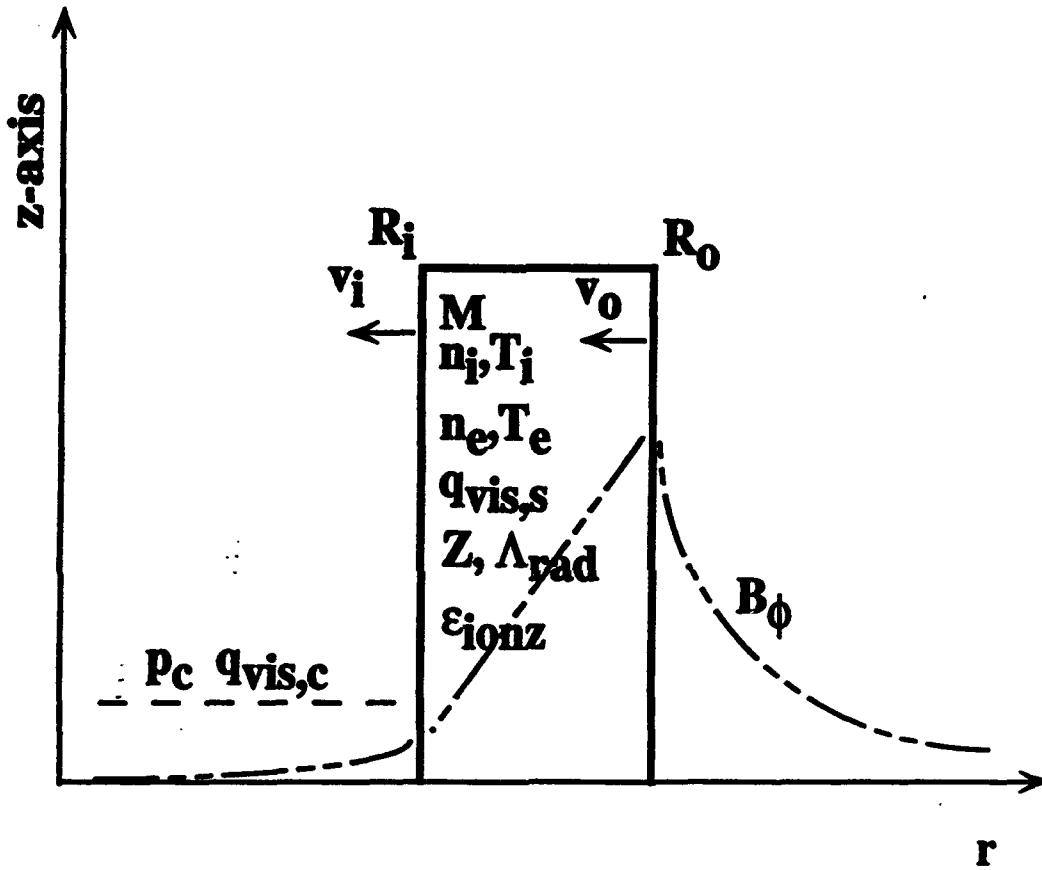


Fig.1 Schematic diagram for the z-pinch modeling in the ZPIMP numerical simulation code. The inner radius R_i , with velocity V_i , and outer radius R_o , with velocity V_o , surround the imploding plasma shell with total mass M , mean ion(electron) density $n_i(n_e)$, mean ion (electron) temperature $T_i(T_e)$, specific ionization/excitation energy ϵ_{ionz} , radiative emission Λ_{rad} , azimuthal magnetic field B_ϕ , and axial current density J_z . The latter two quantities can have a gradient inside of R_o . The region between R_o and the return current radius R_{cc} is a vacuum. The radiationless core region between R_i and the axis has a pressure p_{core} . Both the main plasma shell and the core are subject to an artificial viscosity q_{vis} .

III. Comparison of ZPIMP Calculations with SATURN Al Data

A large set of aluminum wire-array experiments were performed on SATURN over the past few years. The arrays were 2 cm long and consisted of 24 wires of various thickness. The initial load configurations ranged over an order of magnitude in mass and nearly that in array radius. The experimental data including the Al K-shell yield are reported on and compared with radiation scaling law predictions by Whitney, et al. [Ref.1]. In this section an analogous comparison is presented with the ZPIMP code. In terms of an equivalent Thevenin circuit, the SATURN generator has a front end inductance of $L_o = 9.75$ nH and impedance of $Z_o = 0.167\Omega$ [Ref.19]. The circuit and open circuit V_{oc} are displayed in Fig.2. The load mass M , initial radius $R_o(t = 0)$, and length ℓ are chosen to match the experimental data set. To start off the present ZPIMP calculations, the initial load inductance L_{load} of eqn.(12) is fixed at 2.5 nH by adjusting R_o for each specified $R_o(t = 0)$. The inner radius R_i at $t = 0$ is always taken as $3/4 R_o(t = 0)$. The initial temperature for the shell and the core plasma is 5 eV.

Before comparing the yield data with the calculated values, consider the simulation details for the implosion with $M = 0.657$ mg and $R_o(t = 0) = 1.21$ cm. Several properties of the pinch are displayed in Figs.3a – 3d. The inductive notch of the load current (I_{load}) is near the peak of the K-shell radiation pulse in Fig.3a, the minimum of the plasma shell radii in Fig.3b, the maximum shell densities in Fig.3c, and the maximum shell temperatures in Fig.3d. The implosion time can be defined as the difference between two fiducial marks: (i) the intercept of a linear fit to the rising current with the time axis, and (ii) the point of minimum I_{load} during the inductive notch. For the case in Fig.3, the resulting implosion time is ~ 52 nsec. The inner radius never touches the central axis in Fig.3b – the whole plasma shell bounces off the hot inner core during the implosion phase. Note the delay in temperature equilibration between the ions and electrons in Fig.3d. The thermalization of the kinetic energy in the implosion leads first to a rapid and large heating of the ions, characteristic of a strong shock phenomenon. The centroid of the K-shell radiation pulse is shifted toward the expanding phase of the pinch, where the electrons have come into close equilibration with the ions. The mean ionization level in Fig.3b rises to the He-like plateau at ~ 70 nsec and becomes nearly stripped during the highest compression. For this simulation the time integrated radiation power from the aluminum K-shell was 52.5 kJ. The experimental value for the same initial conditions was 63.3 kJ.

Figure 4 displays the K-shell yields, Y_K , from the SATURN data set within circles at the appropriate location in the $R_o - M$ plane. The Y_K value reflects the radiation measured through a $1/8$ mil Kapton filter. The broad coverage of the SATURN data over the $M - R_o$ plane presents a challenging data set to match. Unfortunately none of the shots were repeated, so the intrinsic yield

fluctuation from shot to shot is unknown. In the ZPIMP simulations the viscosity parameter β_{vis} of eqn.(3) was adjusted so that the same value provided a good match to the three experimental shots at $M = 0.657$ mg. For the displayed fit in Fig.4, $\beta_{vis} = 10$. The rest of the simulations were performed then with the same value. The triangles of Fig.4 contain the K-shell yields as calculated from the ZPIMP code using the same initial conditions as the experimental circles to which they are attached. The K-shell yields in the simulations are the sum of all photons above 1.5 keV, which is just below the He- α line of aluminum. One immediately notices the remarkably close agreement between experiments and simulations throughout the $M - R_o$ plane, except to the right of the plot. In this latter region the calculations indicate that the kinetic energy of the plasma at implosion is insufficient to thermalize the entire plasma load into the K-shell ionization stage. In the parlance of Ref.1, these are implosions with $\eta \lesssim 1$. The larger experimental values in this domain compared to those from simulations arise from the presence of large spatial gradients in the plasma at implosion.

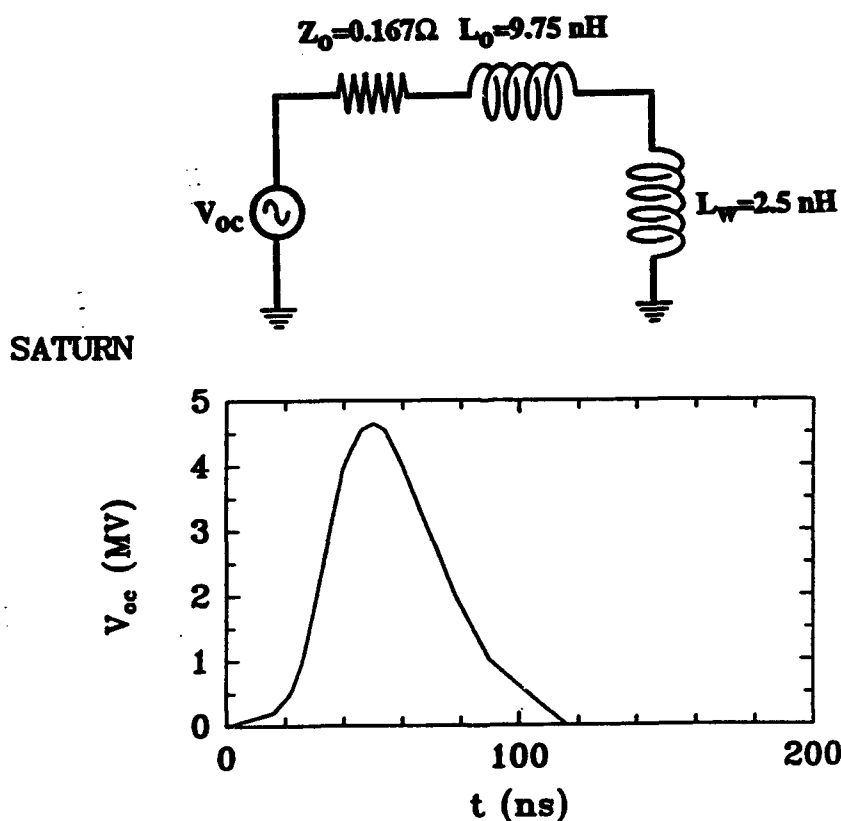


Fig.2 Equivalent Thevenin circuit for the SATURN generator and the open circuit voltage V_{oc} waveform. For the calculations of the present paper the initial load inductance is fixed at 2.5 nH.

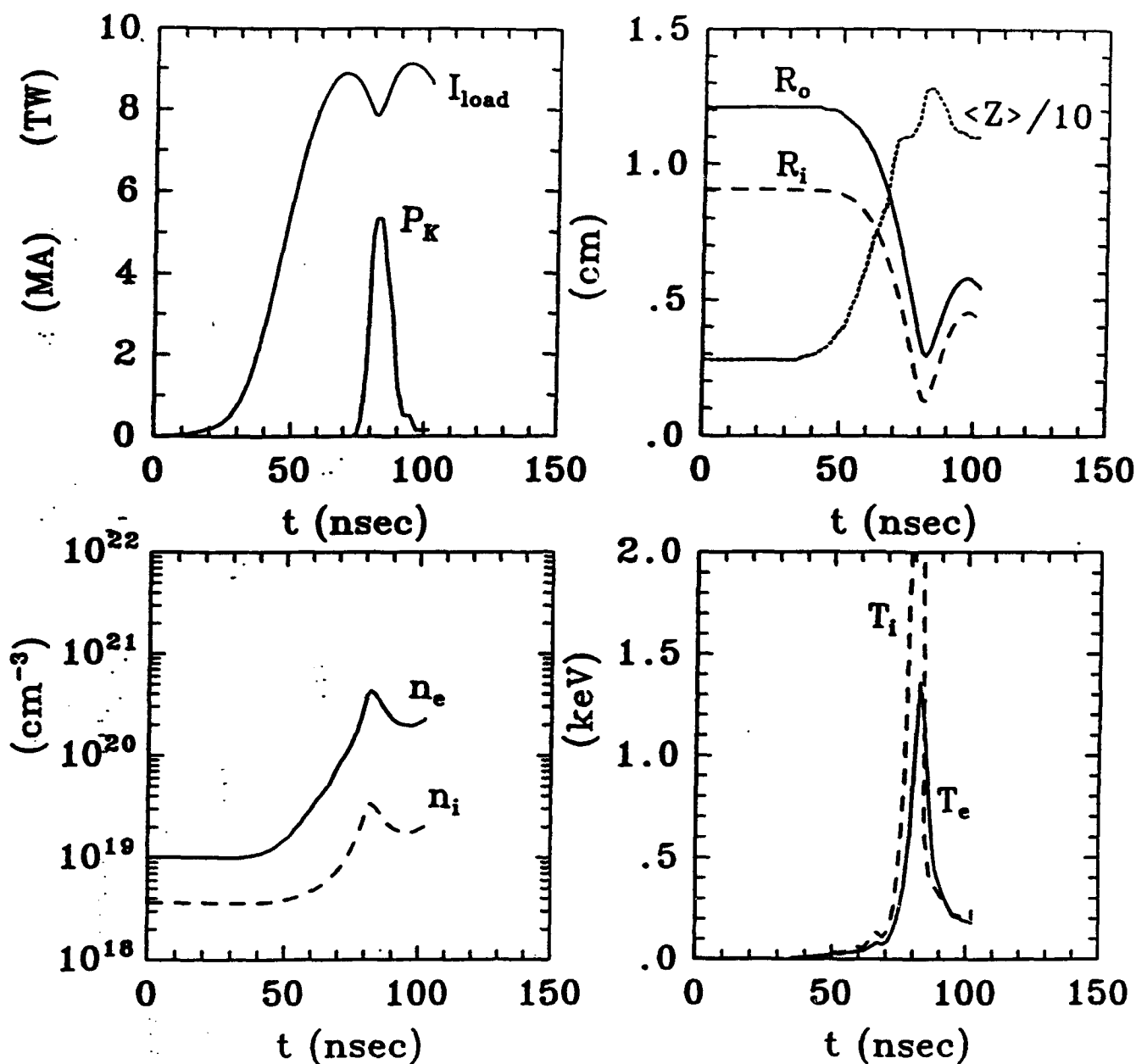


Fig.3 Dynamic features of an aluminum implosion on SATURN from the ZPIMP simulation code. Initial conditions are: $M = 0.657$ mg, initial $R_o = 1.21$ cm, initial $R_i = 3/4 R_o$ cm, and pinch length $\ell = 2$ cm. The viscosity parameter is $\beta_{vis} = 10$. (a) load current and K-shell radiated power; (b) outer and inner radius, with $1/10$ the mean ionization level $\langle Z \rangle$; (c) electron and ion densities; (d) electron and ion temperatures. The calculated K-shell emission is 52.5 kJ while the experimental value for the same initial load configuration was 63.3 kJ.

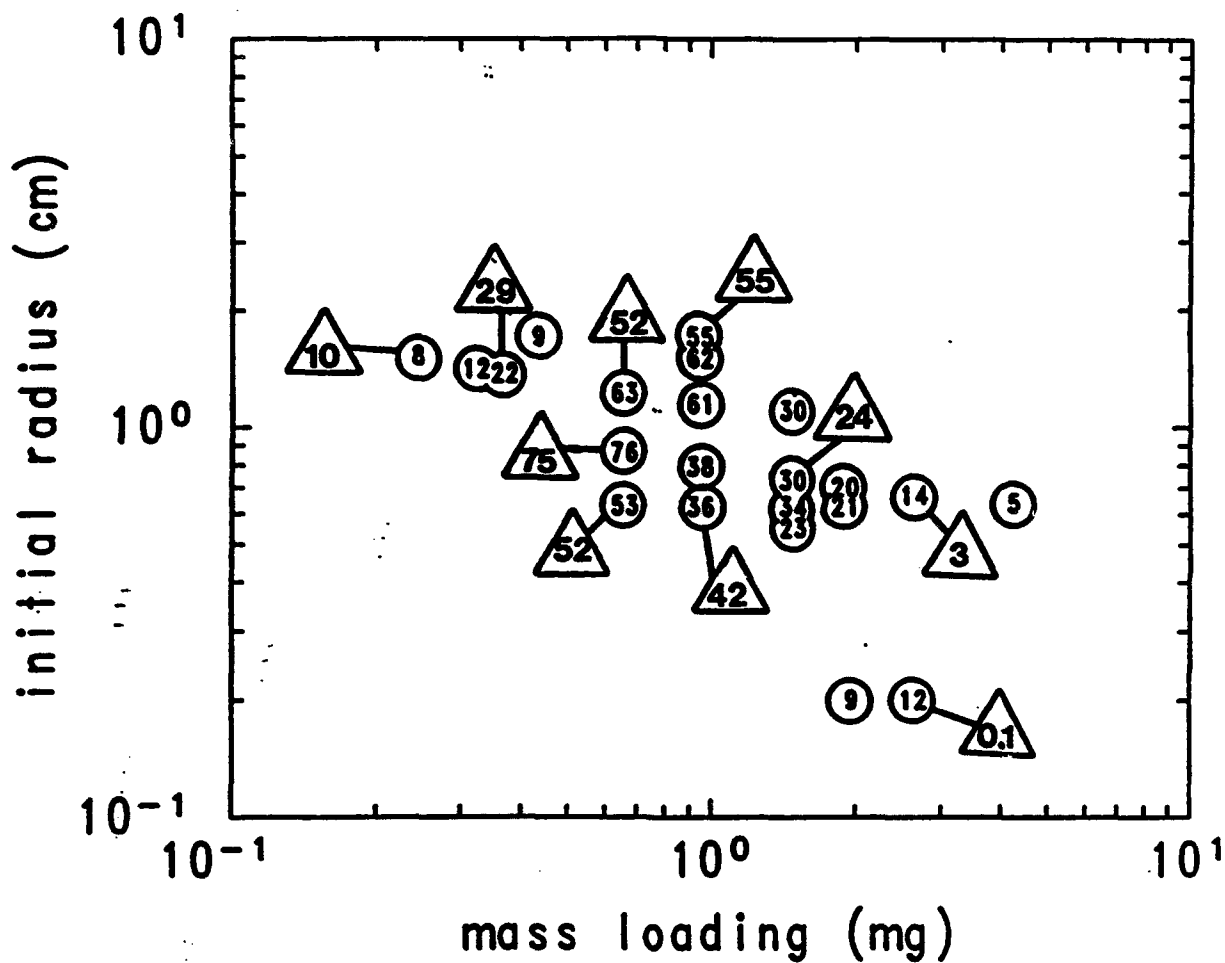


Fig.4 Aluminum K-shell yields for SATURN in the configuration plane of load mass – initial radius. The circles contain the experimental data in kJ from 2 cm long wire arrays. The triangles contain the K-shell yields as calculated from the ZPIMP code using the same initial conditions as the experimental circles to which they are attached. The viscosity parameter $\beta_{vis} = 10$.

IV. Krypton Radiation Yields on a JUPITER-Class Generator

In the present paper an early design version of the linear inductive voltage adder [Ref.20] is used as the JUPITER-class generator. A transmission line code was used to convert the design into an equivalent Thevenin lumped element circuit. The resulting parameters and open circuit voltage V_{oc} for this JUPITER generator is displayed in Fig.5. To study the dependence of the yield over a range of peak load currents we scale the machine through the open circuit voltage, keeping the other circuit parameters fixed. Specifically, the actual open circuit voltage is given by αV_{oc} , with $0.4 \leq \alpha \leq 2$. The corresponding machine will be denoted by LIA-1(α). Hereinafter, the ZPIMP calculations for JUPITER assume $\ell = 4$ cm, $L_w = 2.63$ nH, $R_i(t=0) = 3/4 R_o(t=0)$, and $T_i(t=0) = T_e(t=0) = 5$ eV.

In order to determine the load mass and initial radius conditions leading to the optimal krypton radiation yields it is not practical to perform hundreds of ZPIMP runs, gradually narrowing down the optimal region of parameter space. Instead, a radiation scaling law is used to give a broad brush picture of the K-shell yield dependence in the $M - R_o$ plane. A thin shell model for the pinch dynamics replaces ZPIMP and the implosion is stopped once the circuit has driven the shell to $1/7$ of its initial radius. Details of the procedure are described in Ref.3. Krypton K-shell yield contours for the JUPITER generator LIA-1($\alpha = 1$) are displayed in Fig.6. It suggests that a series of ZPIMP runs to obtain improved yield estimates should be performed with initial radii from 3 to 7 cm and load masses from 10 to 40 mg.

Of the six simulations performed the peak krypton K-shell yield for LIA-1($\alpha = 1$), only 50 kJ, is found at $M = 20$ mg and $R_o = 5$ cm. Consider some details of the dynamics for this simulation. The value for the viscosity parameter β_{vis} is the same as that used to match the SATURN data ($=10$). Fig.7 shows the evolution of the load current, K-shell radiated power, inner and outer radii, mean ionization, ion and electron density, and ion and electron temperature. Measuring the implosion time in a similar way as that described for SATURN, Fig.7a indicates that $t_{imp} \sim 130$ nsec. One can see (Fig.7a) that the inductive notch of the load current has dropped the current from a maximum of ~ 55 MA to ~ 33 MA, the outer radius of the plasma load has decreased only by a factor of ~ 5 , from $R_o(t=0) = 5$ cm to $R_o(t_{imp}) \sim 1$ cm (Fig.7b), and the peak electron temperature (Fig.7d) is ~ 3 keV at implosion. The ion temperature spike in Fig.7d represents the thermalization of the kinetic energy at implosion.

Figure 8 shows the ZPIMP time integrated synthetic spectra for the above simulation run. The forest of narrow emission lines below 5 keV arises from L-shell bound-bound transitions. The recombination edge to the ground state of Li-like krypton lies between these lines and the 5 keV mark. The strong He- α line, a $1s2p(^1P_1)$ to $1s^2(^1S_0)$ transition, is clearly seen at ~ 13 keV. This

energy is the lower end of the K-shell radiation. No other prominent K-shell emission lines are seen for this case. The continuum beyond ~ 17 keV is the sum of free-bound transitions to the He- and H-like ground state. As mentioned above, the K-shell yield, i.e., the integrated emission ≥ 13 keV, for this simulation is 50 kJ. Note that the He- α line is a major contributor to this yield.

In Fig.9 the yields within the various energy bins marked on Fig.8 are shown above the 55 MA peak load current point. The yield in the 15 – 20 keV bin is included in the K-shell yield, but only $\sim 1/2$ of the yield in the 10 – 15 keV bin contributes. To display the trend of yield with load current, a similar search as done above was performed for LIA-1($\alpha = 1/2$) and LIA-1($\alpha = 2$) circuits. For each of these machines, the scaling law was first used as in Fig.6 to provide a rough picture of the yield dependence on the initial load configurations. From these plots a limited set of $M - R_o(t = 0)$ conditions were chosen for further study with ZPIMP simulations. The optimal conditions were found to be $M = 4$ mg, $R_o(t = 0) = 3$ cm for LIA-1($\alpha = 0.4$), and $M = 40$ mg, $R_o(t = 0) = 6$ cm for LIA-1($\alpha = 2$). The calculated yields in the same photon energy bins for these two runs are also presented in Fig.9.

For a JUPITER driver of ~ 60 MA peak load current, one is hoping to achieve much higher yields in the 10 – 15 keV bin than shown in Fig.9. To produce 1 MJ of 10 – 15 keV photons this figure suggests that it is necessary to develop a JUPITER machine which can deliver at least 80 MA peak load current, a formidable task.

The essential problem in producing higher radiation yields is the lack of adequate compression at implosion. The compression ratios of $R_o(t = 0)/R_o(t_{imp})$ in the above JUPITER calculations are similar to the $1/5$ value found in the SATURN simulations. The choice of the viscosity parameter β_{vis} , which essentially controls the compression ratio, was based on matching ZPIMP with the experimental aluminum K-shell yields for SATURN. Suppose it is possible to achieve higher compressions on JUPITER than on SATURN; how would that affect the yields? To study this question requires a harder implosion in the simulations, i.e., one in which the thermalization of kinetic energy is delayed until the pinch is tighter. This means, as far as the simulation modeling is concerned, that the viscosity needs to be lowered. The same M and $R_o(t = 0)$ initial conditions listed in Fig.9 were repeated but with the viscosity parameter β_{vis} reduced to 3 instead of the value 10 used above. The results for the yield variation with load current is presented in Fig.10. An additional point at ~ 40 MA peak load current is also included. The yields in high energy bins above 10 keV have dramatically increased. To reach 1 MJ of 10 – 15 keV photons on LIA-1($\alpha = 1$) now can be achieved with ~ 55 MA peak load current, significantly less than the ~ 80 MA found in the low compression case of Fig.9. The K-shell yields in this high compression scenario are much closer to the scaling law predictions, as contained for instance in Fig.6. The K-shell yield for the $M = 20$ mg, $R_o(t = 0) = 5$ cm run is now 1040 kJ.

To discuss the stagnation physics which is leading to the improved yields, consider the details of the high compression implosion in Fig.11. The initial conditions ($M = 20$ mg, $R_o = 5(t = 0)$ cm) are the same as shown for the low compression case shown in Fig.7. Though the same peak load current is reached, note the deeper inductive notch in Fig.11a and the associated deeper implosion in Fig.11b. Because the viscosity is lower than in Fig.7, the bounce is harder and the peak kinetic energy is larger: ~ 11 MJ in the high compression case compared to ~ 8 MJ in the low one. In both cases the ion temperature shoots up to tens of keV at thermalization, but the peak electron temperature is ~ 5 keV for high compression case (Fig.11d), and only ~ 3 keV for the other (Fig.7d). Furthermore, the electron densities are in the ratio $n_e(\text{high})/n_e(\text{low}) = \sim 5$ from Figs.7c and 11c. Together, these factors lead to a shorter ion-electron equilibration time,

$$\tau_{ie} \propto \frac{T_e^{3/2}}{\langle Z \rangle n_e}, \quad (13)$$

for the high compression case. This is consistent with the more rapid equilibration and higher peak T_e evidenced in Fig.7d.

The impact upon the K-shell yield due to the larger n_e and T_e for the high compression case can be seen by noting the formula for the He- α emission rate:

$$\frac{\text{photons}}{\text{sec}} \propto n_{He} n_e \frac{e^{-13(\text{keV})/T_e}}{T_e^{1/2}}, \quad (14)$$

where n_{He} is the He-like ground state density of krypton. This equation is valid in the limit of coronal equilibrium where every upward excitation to the excited state is followed by a radiative decay. To attain the opposite extreme of local thermodynamic equilibrium in the K-shell of krypton requires $n_e \sim 10^{28} \text{ cm}^{-3}$, which far exceeds the peak n_e in Fig.11c. This large value follows from the corresponding required electron density for aluminum (10^{25}) [Ref.21] and the Z_{nuc}^7 scaling to other elements [Ref.22]. Using the above values for T_e and n_e leads to a factor of ~ 20 enhancement in the He- α bound-bound photon production rate for the high compression case compared to that for low compression. This factor would be even larger if the slight increase in mean ionization of Fig.11b over that in Fig.7b were taken to indicate a slightly enhanced n_{He} for the high compression case. Given that the K-shell pulse widths in Fig.7a and 11a are nearly the same, and the dominance of the He- α contribution to the total K-shell yield for this implosion, the factor of ~ 20 explains the ratio in the K-shell yield of the two cases: $Y_K(\text{high})/Y_K(\text{low}) = (1040 \text{ kJ})/(50 \text{ kJ})$.

Thus the large difference in the yield is due to moderate changes in the plasma conditions during the thermalization phase, i.e., the faster temperature equilibration coupled with the enhanced electron density of a higher compression. As pointed out in the first paper in this series on scaling

law estimates of JUPITER yields [Ref.3], the optimal yielding implosions for krypton on JUPITER are weak implosions in the sense that the kinetic energy is barely sufficient to thermalize the whole plasma into the K-shell ionization stage. Using η as the ratio of the kinetic energy per particle over the energy needed to ionize the atom to a 50%He- 50%H-like configuration [Ref.4], these implosions have $\eta \lesssim 1$. Such implosions were only crudely treated by the J-scaling law described in Ref.3, and the present results of Figs.9 and 10 attest to the sensitivity of the yields arising from the complexity of the stagnation physics.

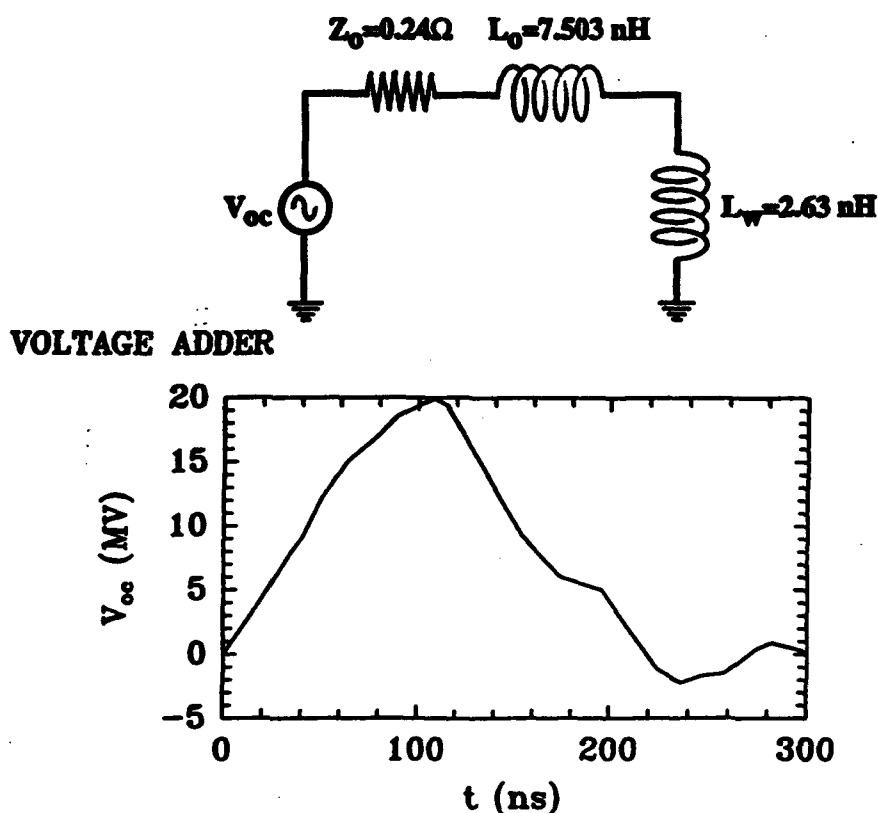


Fig.5 Equivalent Thevenin circuit for a JUPITER generator. The circuit is based on an early version of the linear inductive voltage adder, hereinafter called LIA-1. For the calculations of the present paper the initial load inductance is fixed at 2.63 nH and the pinch length is 4 cm. For different machine versions the amplitude of the open circuit voltage is multiplied by a parameter α between 0.4 and 2. The corresponding version is termed LIA-1(α).

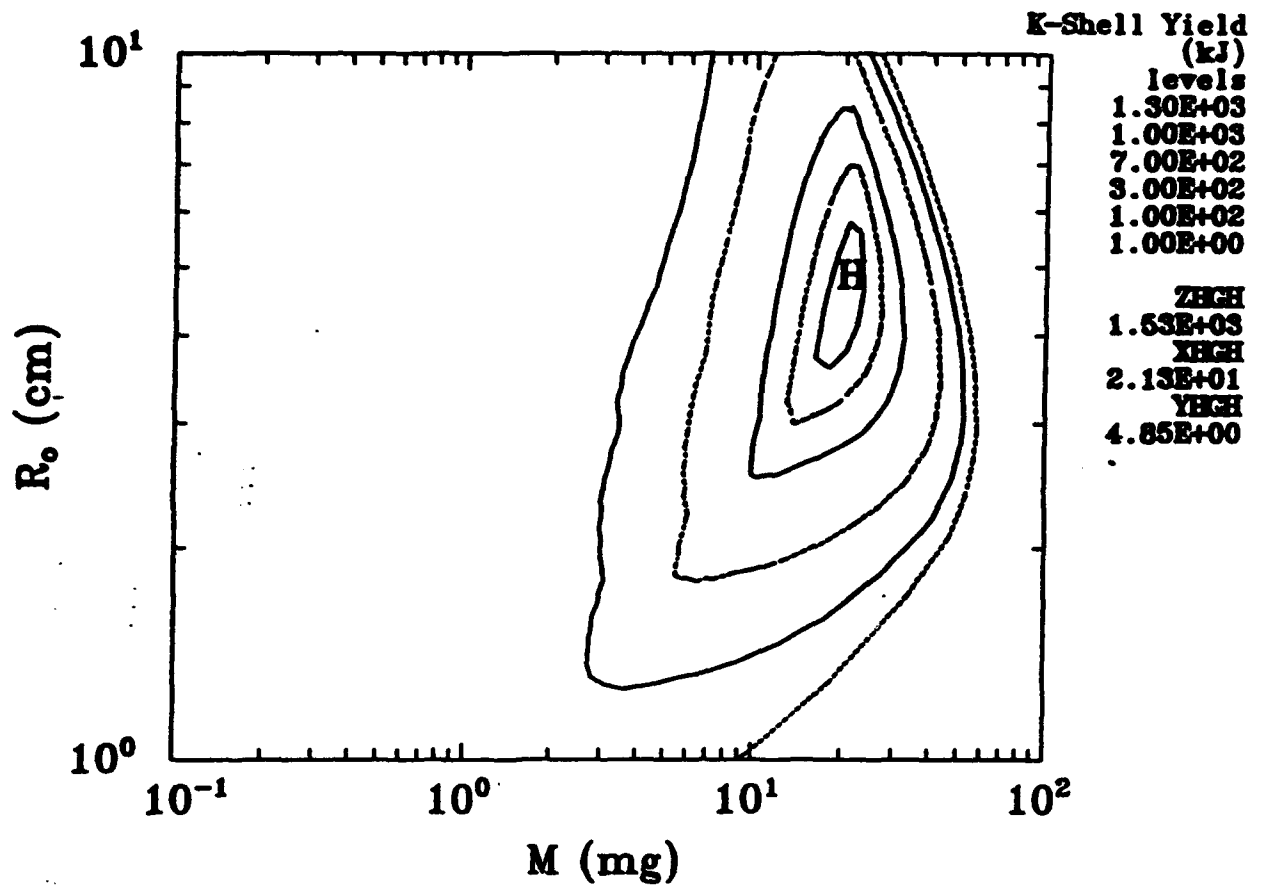


Fig.6 Yield contours in the load mass initial radius plane for krypton K-shell radiation. The yields are based on a combination of the thin shell dynamics for the load, the LIA-1($\alpha = 1$) design of Fig.5, and the K-shell J-scaling law of Ref.3. The implosion is stopped at $1/7$ of the initial radius. This graph suggests the region of initial conditions where ZPIMP calculations can focus on improved yield estimates.

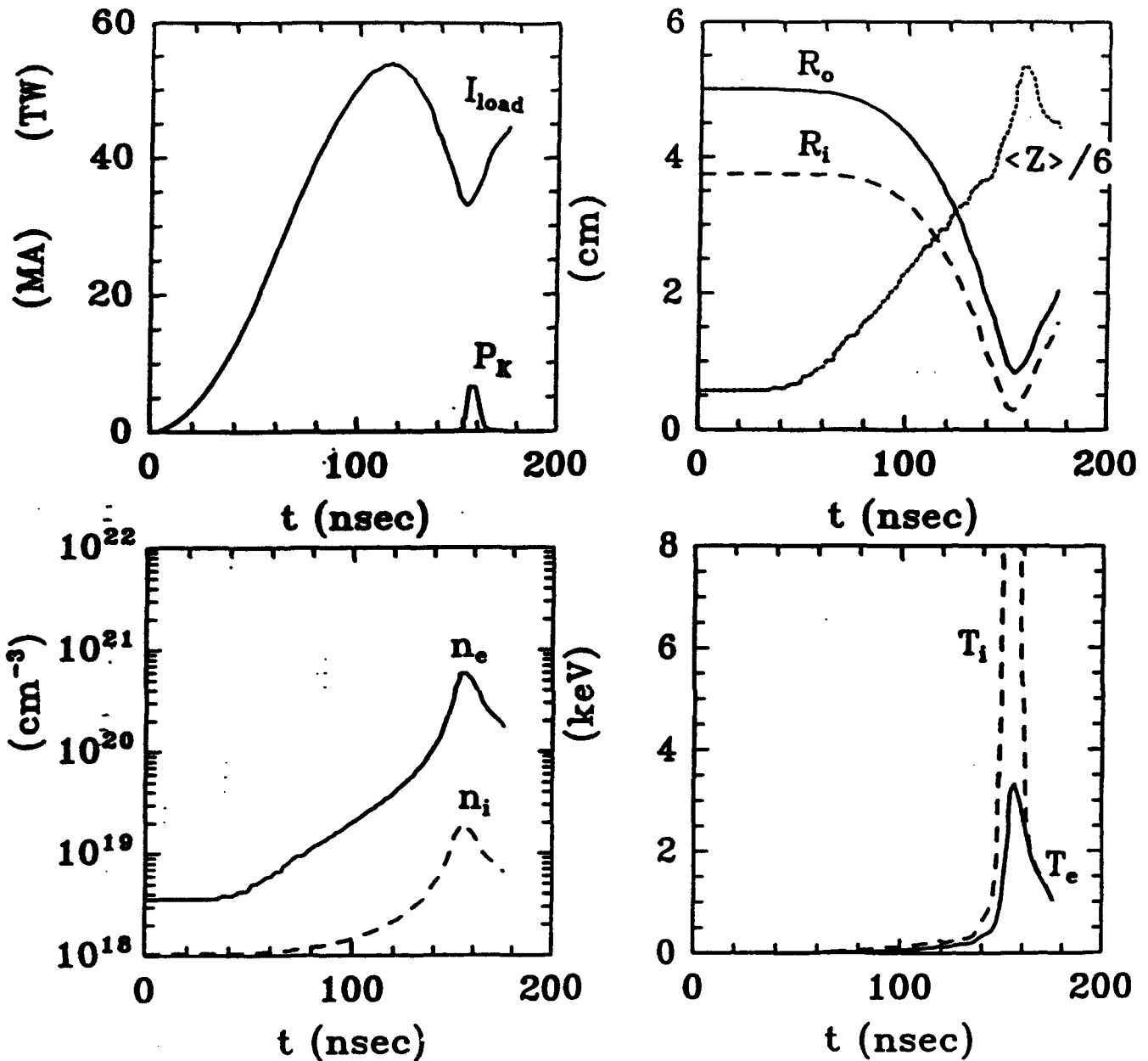


Fig.7 Dynamic features of a krypton implosion on the JUPITER circuit LIA-1($\alpha = 1$) from the ZPIMP simulation code. Initial conditions are: total mass $M = 20$ mg, initial $R_o = 5$ cm, initial $R_i = 3/4 R_o$ cm, and pinch length $\ell = 4$ cm. The viscosity parameter ($\beta_{vis} = 10$) is chosen to give a similar compression ($1/5$) as used to match the SATURN data in Fig.4. (a) load current and K-shell radiated power; (b) outer and inner radius, with $1/6$ of the mean ionization level $\langle Z \rangle$; (c) electron and ion densities; (d) electron and ion temperatures. The calculated K-shell emission is 50 kJ.

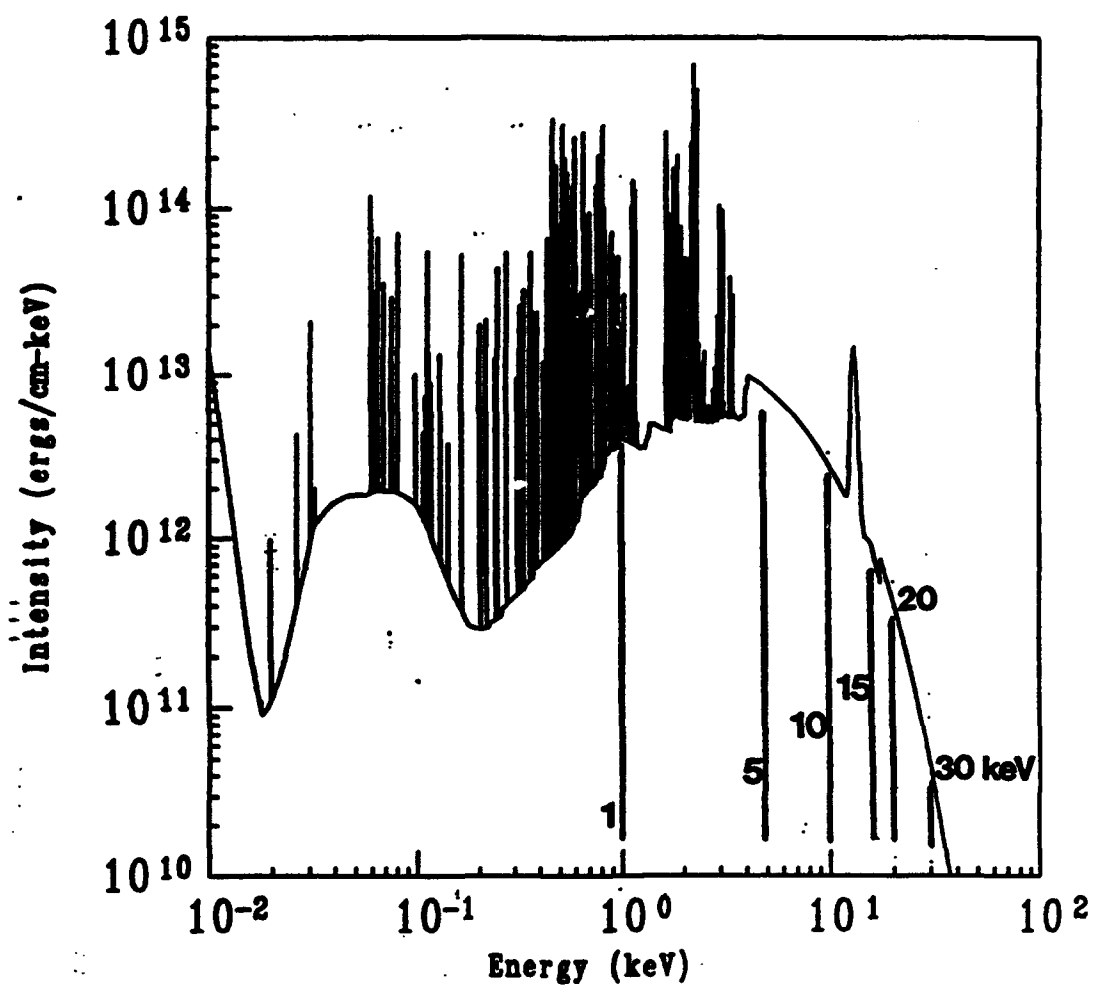


Fig.8 Time integrated synthetic ZPIMP spectra from the krypton simulated implosion described in Fig.7.

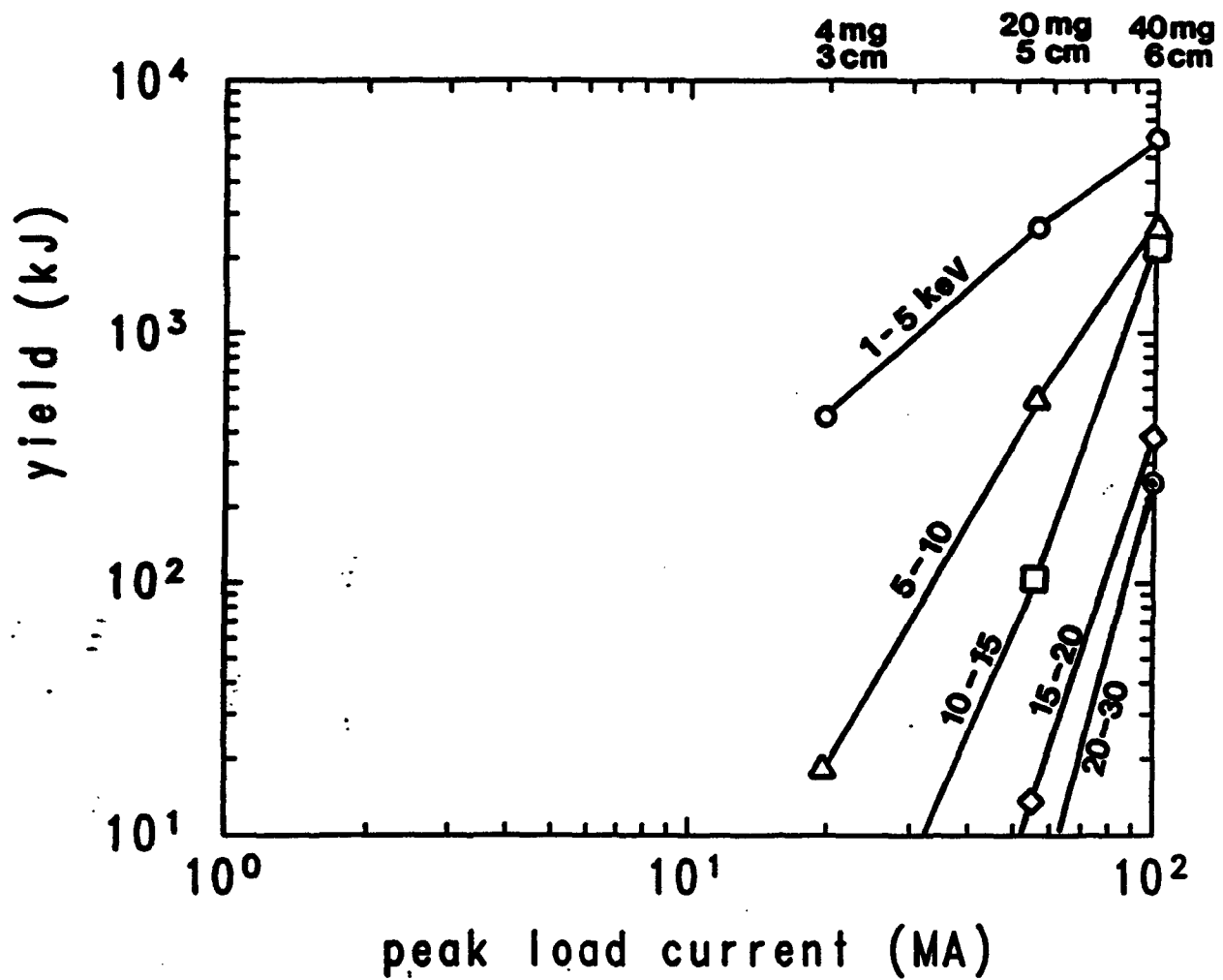


Fig.9 Krypton yields vs peak load current in various photon energy bins for the circuits LIA-1($\alpha = 0.4, 1.0, 2.0$). The load mass and initial radius for the different implosions are shown at the top. The viscosity parameter ($\beta_{vis} = 10$) for this case leads to low compressions where $R_o(t_{imp})/R_o(t = 0)$ is $\sim 1/8$.

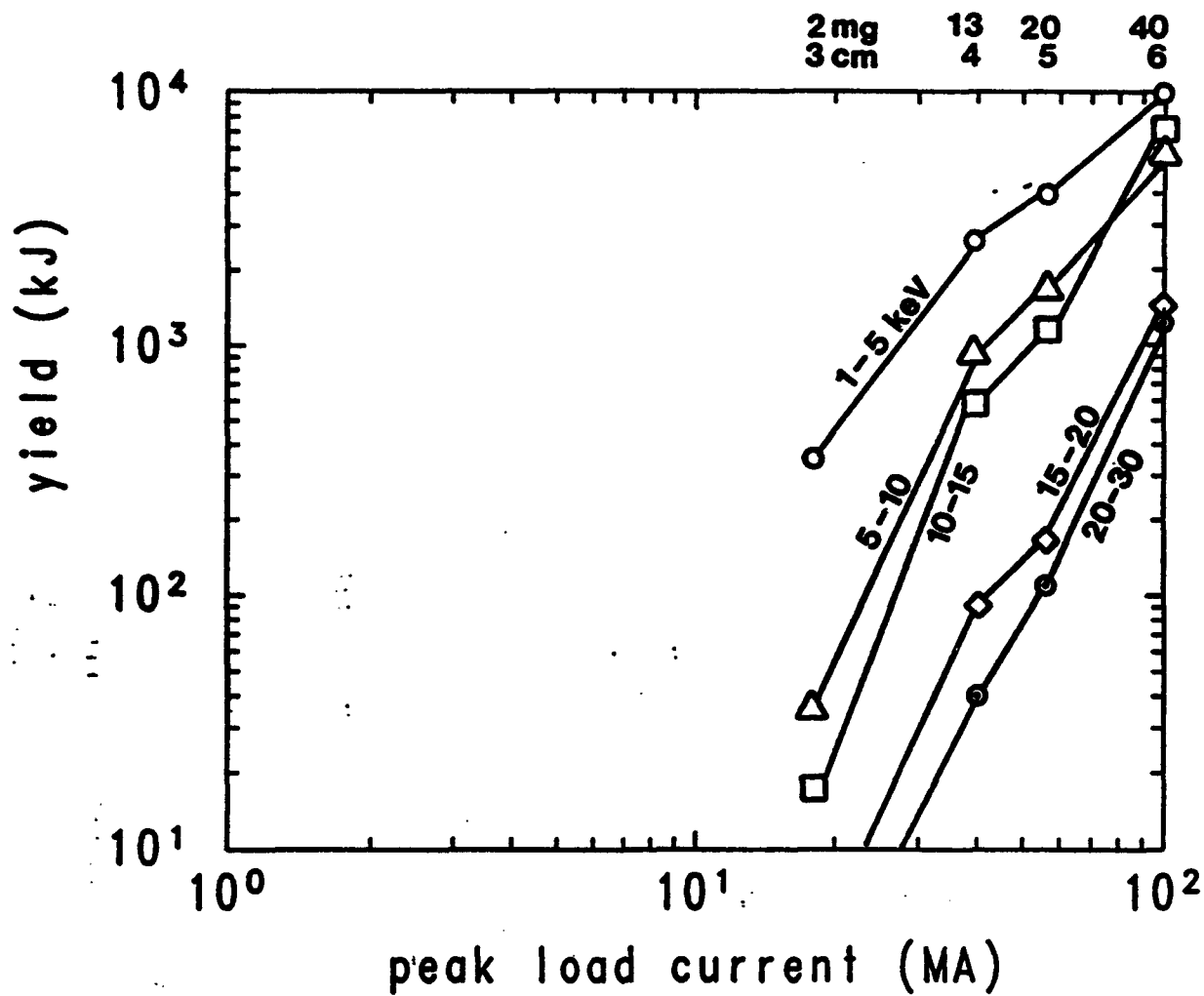


Fig.10 Krypton yields vs peak load current in various photon energy bins for the circuits LIA-1($\alpha = 0.4, 1.0, 2.0$). The load mass and initial radius for the different implosions are shown at the top. The viscosity parameter ($\beta_{vis} = 3$) for this case leads to high compressions where $R_o(t_{imp})/R_o(t = 0)$ is $\sim 1/10$.

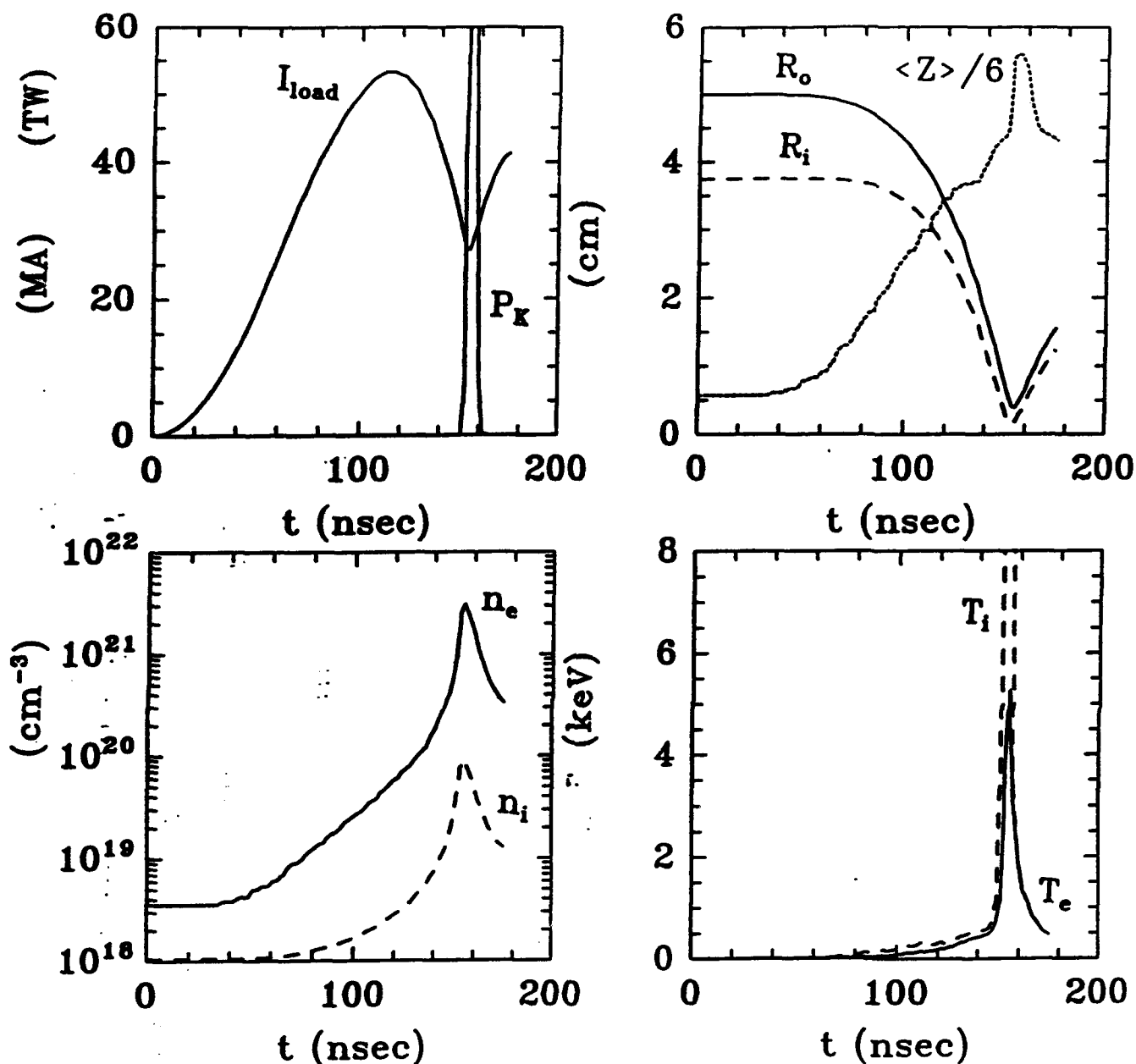


Fig.11 Dynamic features of a krypton implosion on the JUPITER circuit LIA-1($\alpha = 1$) from the ZPIMP simulation code. Initial load conditions are the same as in Fig.7. The viscosity parameter ($\beta_{vis} = 3$) is chosen to give a higher compression ($\sim 1/10$) than in Fig.7. (a) load current) and K-shell radiated power; (b) outer and inner radius, with $1/6$ mean ionization level $\langle Z \rangle$; (c) electron and ion densities; (d) electron and ion temperatures. The calculated K-shell emission is 1040 kJ.

V. JUPITER Capabilities vs. Radiation Requirements

The final task before us is to use the ZPIMP simulation code to predict JUPITER yields in various energy bins and compare the results with stated radiation testing requirements. Table I lists radiation fluence requirements for simulator testing and the corresponding source yields resulting from fluence uniformity on target. The impact on source yield due to various standoff distances imposed by debris shielding is presented in Table II. Table III lists the optimal yields in the energy bins from argon, krypton, and xenon calculated with the ZPIMP code for the JUPITER-class machine LIA-1($\alpha = 1$) of Fig.5. A detailed description of the tabular columns follows.

From T. Kennedy's presentation at JDOST-3 [Ref.23] the fluence requirements of Table I are separated into five photon energy bins, denoted by the letters A - E. The bin nomenclature and energy limits are listed in the first two columns. Cases D and E have been amended to include an upper bound on the photon energy. The minimal requirements from T. Kennedy of fluence on the target surface, target area, and uniformity are given in the third through fifth column, respectively. Assume that the target presents a disc normal to the line of sight from the source. The radius of such a disc, r , is readily computed in column six from the stated area. Let D be the distance from the source to center of the target, u the uniformity requirement, and t the filter transmission factor. The geometry is depicted in Fig.12. If Y is the source radiation yield, the fluence at the center of the target is

$$F_{center} = t \frac{Y}{4\pi D^2}, \quad (15)$$

while the fluence at the target edge is

$$F_{edge} = t \frac{Y}{4\pi(D^2 + r^2)} \cos \theta. \quad (16)$$

The angle θ arises from the fact that the radiation from the source striking the edge of the target is at an angle to its surface normal. Since the target was assumed flat, the angle is the same as that subtended by the target at the source. Because the target shapes may not be flat, results in Table I are given with and without the angle correction. To satisfy the uniformity requirement one must have $F_{edge} \geq u F_{center}$, and the minimum distance which can satisfy this requirement, neglecting the angle term in eqn.(16), is

$$D_{min} = r \sqrt{\frac{u}{1-u}}. \quad (17)$$

On the other hand, if the angle term is included and one notes that $\cos \theta = D/\sqrt{D^2 + r^2}$, then

$$\left(\frac{D_{min}}{r}\right)^3 = u \left[\left(\frac{D_{min}}{r}\right)^2 + 1 \right]^{3/2}. \quad (18)$$

The resulting D_{min} are listed in columns seven and eight and show that the angle factor can make a significant difference. Given the transmission factor of column nine, and the distances of columns seven and eight, the minimum required source yield in each energy bin is presented in the last column of Table I. For comparison, we note that the largest K-shell yields to date, 76 kJ above 1 keV, has been achieved on SATURN with Al wire array implosions. An improvement of a factor of ~ 22 is needed by JUPITER just to meet the minimum yield requirement for case B.

The minimum distance for uniformity of Table I does not, however, account for the physical apparatus needed to protect the target from particulate debris. This apparatus, with its shields and fast valves, imposes a physical separation between the source and the test object which is termed the debris mitigation distance. The mitigation apparatus for a JUPITER class generator demands a significant R & D effort. Anticipating future technology improvements, Table II includes an estimated range for the debris mitigation distance in column five. The five test cases A - E, their energy bins, required fluences, and transmission factors are also repeated in the first four columns of Table II. Based on the fluence and transmission factor, and the min/max range in debris mitigation distance, the required source yields can readily be calculated from eqn.(15). These are presented as ranges in the corresponding bins in the last column of Table II. Clearly there is a lot to be gained in terms of the required yields if the R & D on debris mitigation can reduce the standoff distance. Note that the minimum debris mitigation distance for some of the cases A - E is smaller than the corresponding minimum distance for uniformity based on eqn.(18) and listed in Table I. On the other hand, if the angle between the radiation and the target normal is unimportant, the uniformity condition is automatically satisfied by comparing the distances of column seven of Table I and those in column five of Table II. A further discussion of this issue is given by Hedermann in the Final JDOST Report [Ref.24].

Given the source requirements of Table I or Table II, what can one expect in the various energy bins from a JUPITER-class generator? An answer to this question can be provided by using ZPIMP to calculate the radiation yields from specific load configurations. The specific JUPITER design used in the calculations is that of Fig.5, with $\alpha = 1$. As above, a general view of the yield dependence on initial radius $R_o(t = 0)$ and load mass M was created by using the K-shell J-scaling law [Ref.3] on this generator for argon, krypton, and xenon. Once the promising region in the $M - R_o$ was determined (the pinch length was fixed at 4 cm), ZPIMP runs were performed for a limited set of conditions within this region and the optimal configuration was sought. For argon and krypton the ionization dynamics was treated with a DCA model as described in Section II; for xenon, the AA model. Because the compression of the pinch based on the viscosity parameter β_{vis} was found to be very important in the krypton yields of Section IV, both low compression ($\beta_{vis} = 10$) and high compression ($\beta_{vis} = 3$) runs were made. The optimal material, load

configurations, and calculated yields are presented for each radiation bin in Table III. Note the large yield improvements with the high (column eight) over the low (column seven) compression cases, especially for bins C through E. As explained in the previous section, this difference reflects the higher electron densities, faster thermal equilibration, and enhanced K-shell emission of the high compression runs compared with the low.

The final two columns of Table III repeat the range of required yields: column nine from the last column of Table I; column ten from the last column of Table II. The values in column nine are based on eqn.(18), i.e., the $\cos \theta$ term of eqn.(16) is included. The maximum in the projected range of required yields (columns nine and ten) is clearly that arising from the largest debris mitigation distance – the upper value of the last column in Table III. The minimum in the same projected range is from column nine for bins A – C, and the lower value of the last column for bins D and E. The last four columns of Table III offer a direct comparison between predicted capabilities and anticipated requirements for the source yield on JUPITER. For bin A, even the simulation with low compression exceeds the largest yield requirement. The radiation in this lowest energy photon bin is entirely from argon L-shell continuum and line emission. The plasma T_e need only be a couple hundred eV to radiate efficiently in the 0 – 1 keV regime, i.e., the photon output is not tied to a large implosion velocity. Hence a large load mass can be used to boost the yield. For bin B, only the required yield for the largest debris mitigation distance is beyond the predicted krypton capabilities for low or high compression. The next bin, C, presents a transitional situation: The low compression krypton yields are below all of the required yields, while the opposite holds for the high compression case. For the high energy bins D and E, both the low and high compression simulations for krypton and xenon give yields below the range of required values, though the high compression krypton yield for bin D, 280 kJ, is close to the required yield if the minimum debris mitigation distance is realizable.

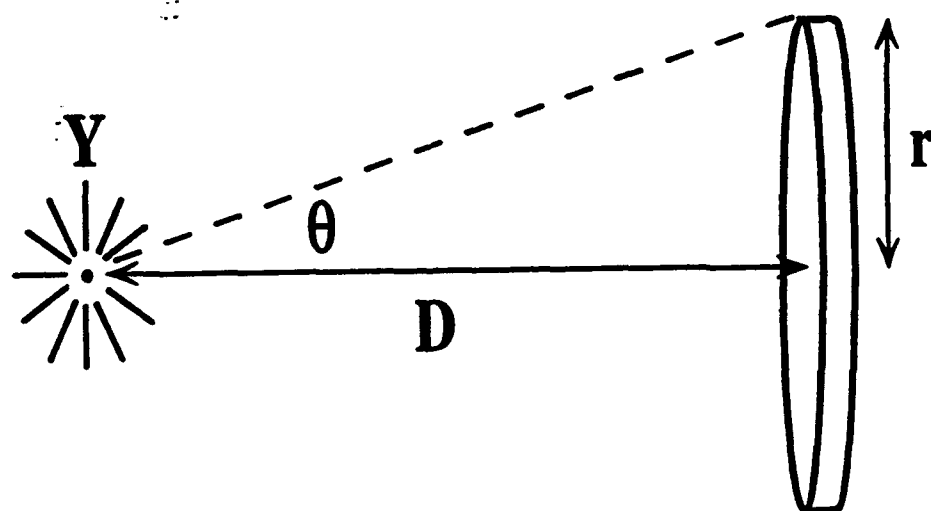


Fig.12 Geometry used to transpose a radiation fluence requirement at a target of area A into an yield requirement Y from a point source a distance D away.

Table I. Minimum Yields for Uniformity

	photon bin (keV)	required fluence (cal/cm ²)	required test area (cm ²)	required fluence uniformity	test radius (cm)	minimum distance [eqn.(17)] (cm)	minimum distance [eqn.(18)] (cm)	filter transmission factor	required source yield (uniformity) (kJ)
A	0 - 1	1	25,000	80%	89.2	178.4	222.7	0.8	2093-3261
B	1 - 5	1	20,000	80%	79.8	159.6	199.3	0.8	1675-2612
C	5 - 15	1	10,000	80%	56.4	112.8	140.8	0.8	837-1304
D	15 - 30	5	60	90%	4.4	13.2	16.3	0.8	57-87
E	30 - 60	5	25	90%	2.8	8.4	10.4	0.8	23-36

Table II. Minimum Yields for Debris Mitigation

	photon bin (keV)	required fluence (cal/cm ²)	filter transmission factor	min - max debris mitigation distance (cm)	required source yield (debris) (kJ)
A	0 - 1	1	0.8	200 - 300	2630 - 5918
B	1 - 5	1	0.8	180 - 270	2130 - 4793
C	5 - 15	1	0.8	125 - 190	1027 - 2374
D	15 - 30	5	0.8	30 - 50	296 - 822
E	30 - 60	5	0.8	20 - 40	132 - 526

Table III. ZPIMP Voltage Adder Simulations [LIA-1($\alpha = 1$)]

	photon bin (keV)	material	mass (mg)	initial radius (cm)	pinch length (cm)	low compression source yield (kJ)	high compression source yield (kJ)	required source yield (uniformity) (kJ)	required source yield (debris) (kJ)
A	0 - 1	Ar	60	3	4	7820	11000	3261	2630 - 5918
B	1 - 5	Ar	20	3	4	3060	4390	2612	2130 - 4793
C	5 - 15	Kr	20	5	4	609	2570	1304	1027 - 2374
D	15 - 30	Kr	10	5	4	17	280	87	296 - 822
E	30 - 60	Xe	5	5	4	-	50	36	132 - 526

VI. Summary and Conclusions

In a previous paper on the JUPITER PRS scoping study we noted three fundamental load issues: stagnation physics, high Z ionization dynamics, and stability. These rendered the predicted K-shell yields from the J-scaling law uncertain. The present report was focused on providing an improved estimate for yields in specific energy bins by using a 1-D radiation-magnetohydrodynamic code, ZPIMP, to simulate implosions on one JUPITER circuit. The ZPIMP code addressed the first two of the above issues: stagnation physics by following the load dynamics from some early ionized phase through the implosion and bounce, and ionization/excitation dynamics by using a detailed atomic physics package with self-consistent radiation transport. This model was coupled to a simple lumped circuit for the JUPITER driver. The advantage of ZPIMP is its simple treatment of the plasma load as a single zone or shell. There are separate momentum equations for the inner and outer shell radii, a single ion internal energy equation, and a single electron internal energy equation (Fig.1). Since the computation time for radiation transport scales faster than the square of the number of zones, this single zone approach offers expediency in calculation. In our study of SATURN implosions it was found necessary to include a non-radiating, low density, inner zone which developed into a hot core at implosion.

The viability of ZPIMP was investigated by comparing the aluminum K-shell yields from z-pinch experiments on SATURN with ZPIMP simulations. The results, in the initial load configuration ($M - R_o$) plane of Fig.4, showed excellent agreement with the data, except in the region of weak implosions where the kinetic energy is insufficient to ionize the entire plasma into the K-shell. The viscosity parameter β_{vis} of the simulations ($= 10$) was determined by matching three of the data points and then using the same value for the remainder of the simulations. A detailed study of one of the implosions in Fig.3 indicates a typical compression ratio $R_o(t_{imp})/R_o(t = 0)$ of $\sim 1/5$.

In order to calculate radiation yields from a JUPITER-class generator, an early version of the linear inductive voltage adder (LIA-1) was converted to an equivalent Thevenin circuit (Fig.5). The circuit was used to represent more and less energetic machines by scaling the open circuit voltage ($= \alpha V_{oc}$) while keeping the other circuit parameters fixed. This enabled us to look at the yield dependence as a function of the peak load current. For each machine version, termed LIA-1(α), a search was performed in the $M - R_o$ plane to find optimal yielding conditions. A typical implosion dynamics was presented in Fig.7. The time integrated spectra (Fig.8) was divided into various energy bins and the yield in each bin was plotted in Fig.9, along with the optimal yields for the other machine versions. This figure showed disappointing yields, and to improve them the β_{vis} parameter, initially set to match the SATURN data ($=10$), was lowered to 3 to obtain higher

compressions. The high compression yields in Fig.10 were significantly improved. Comparison of the dynamics for the high compression case (Fig.11) with the same load conditions but low compression (Fig.7), demonstrated that the yield improvement was due to a speedier equilibration of the electron temperature in conjunction with a higher electron density at implosion. The moderate changes led to a factor of ~ 20 enhancement of the total K-shell yield, most of it coming from the He- α line emission. This result pointed out the significance of stagnation physics modeling for those implosions with $\eta \sim 1$

Finally, the ZPIMP code was used to estimate optimal yields in the energy bins listed in the requirements for JUPITER. This search was performed for LIA-1($\alpha = 1$) of Fig.5 over the pinch materials argon, krypton, and xenon. The stated fluence requirements in each photon energy bin was converted to a required source yield, first by satisfying the fluence target uniformity requirement (Table I), and then using an estimate for the debris mitigation distance (Table II). Comparison with projected yields from the JUPITER design model were given in Table III. Anticipating improvements in load physics understanding and control, high implosion [$R_o(t_{imp})/R_o(t=0) \sim 1/10$] as well as low implosion ($\sim 1/5$) cases were reported. In the lower energy bins, A (0 – 1 keV) and B (1 – 5 keV), the calculated yields from either compression case are close to or exceed those required. This reflects the fact that for argon, JUPITER implosions can reach the efficient scaling regime where the yield scales with load kinetic energy. But in the highest bins, D(15 – 30 keV) and E (30 – 60 keV), the present calculations indicate that predicted yields fall short of the required ones. Here, the implosions are in the low η regime and the subsequent yields are susceptible to the details of the stagnation physics, such as temperature equilibration as shown above.

Both the previous report and the present one predict that low Z elements will be efficient radiators on a JUPITER-class generator in the 0 – 1 and 1 – 5 keV photon energy bins. The optimal K-shell yields of aluminum (≥ 1.6 keV) and argon (≥ 3.1 keV) are consistently projected with the J-scaling law, as well as ZPIMP simulations, to be $\sim 30\%$ of the load kinetic energy. But these reports cannot be viewed as the end of theoretical research on JUPITER PRS loads. Firm predictions for JUPITER's yield capability above 10 keV are not in hand due to a number of load physics and related simulation modeling issues. Five of these issues are discussed next.

(i) The present report noted that the pinch could not be treated as a plasma shell imploding through a vacuum onto the axis. It was found necessary to include a core plasma which heats up and contributes to the softening of the primary load's collapse on axis. Experimental evidence for early plasma formation on axis was noted by Aivazov [Ref.9] for aluminum wire loads. These authors also suggested that the blowoff from each wire during the initial current rise subsequently collapses prior to the main plasma mass due to its low density. Other theoretical analyses by

Bloomberg, et al., [Ref.25] led to the conclusion that one does not expect the later evolution of the wire plasma to be dependent upon initial conditions. However, a re-investigation of this problem by Whitney, et al. [Ref.26] using a similar approach, found that SATURN kilovolt yields vary directly with the theoretical temperatures achieved in the early wire explosion phase of the pinch dynamics. Indirect evidence also exists for the importance of a pre-formed core plasma and enhanced transport coefficients for argon gas puffs [Ref.10]. The simulations in this reference, which were matched to experimental pinch densities and temperatures at implosion, suggest that the primary load bounces off a hot core rather than collapsing all the way to the axis. The origin of the core plasma for gas puffs reflects the initial density distribution arising from the nozzle jet, i.e., the region within the gas puff shell is not a vacuum. The wire array diagnostics, the detailed analysis of argon gas puffs, and the present study to match a large set of SATURN data all point to the potentially important influence of the *startup phase* for pinch dynamics. The response of the early wire blowoff or gas puff density profile to the larger dI/dt of JUPITER compared to present machines is presently unknown. These aspects need detailed investigation, especially since a pre-formed, axial plasma would hinder the potential for high compression [$R_o(t=0)/R_o(t_{imp}) \gtrsim 10$] pinches. Based on the LIA design in this report, such pinches were found to be essential if one hopes to match the radiation requirements in the photon energy bins above 5 keV.

(ii) In order to achieve copious amounts (\geq MJ) of high energy photons (≥ 10 keV) it will be necessary to implode high atomic number ($Z_{nuc} > 18$) material to sufficiently high velocity that it is ionized into the K-shell stage upon thermalization. For JUPITER designs which reach ~ 60 MA peak load current this means that the implosions will not have enough kinetic energy to thermalize the bulk of a high Z load into the K-shell, or it will not carry sufficient mass to radiate efficiently. In the parlance of Ref.3, optimal radiating loads on JUPITER have $\eta \sim 1$ for krypton, and $\eta < 1$ for xenon. The present ZPIMP study of krypton on a JUPITER-class generator clearly demonstrated the sensitivity of krypton K-shell yields to moderate changes in the mean plasma density and temperature at implosion. It should also be obvious that the high energy radiation yield will be susceptible to plasma gradients at implosion, not only because distinct regions of the plasma will radiate differently than the average conditions, but also because radiation transport depends upon local gradients. The potential for stability and enhanced yields through innovative load designs can be ascertained only if the details of the plasma dynamics are properly treated. This includes *a better understanding through experiments and modeling of the instabilities, zippering, enhanced transport coefficients, and general turbulence acting in the plasma* to soften the implosion [Ref.5] and broaden the radiation pulse width. The present phenomenological treatment of this stagnation physics through the viscosity parameter β_{vi} , tied to SATURN data makes the extension of the model to JUPITER load currents uncertain. Research is under way to see if the comparisons

with SATURN made in Fig.4 lead to similar viscosity models for the other existing pulsed power generators: PHOENIX, BLACKJACK 5, DOUBLE EAGLE. Altogether, these comments make the case for load studies with multi-zone 1-D and 2-D simulations which concentrate on the plasma profiles during implosion. Initial work on 2-D stability has begun [Ref.27], but it is a large undertaking for the details depend on the history of the pinch when coupled to the driver.

(iii) Not only is the plasma dynamics important in high Z , low η implosions for the high energy photon yields mentioned in (i) and (ii) above, so is the *atomic physics and ionization/excitation dynamics*. For high Z_{nuc} radiators, the pre-implosion radiative losses through L- and even M-shell emission rob from the implosion energy and thereby lower the ionization level at thermalization. A systematic investigation into the krypton yield dependence on the modeling of the L-shell was presented by Davis [Ref.28] at the second JDOST meeting. Both the krypton DCA model used in the present work and the one in Ref.28 should be amended with an extensive M-shell model. Improvements to the atomic physics model for krypton are straightforward, but time consuming in code updating. For xenon, the potential pre-K-shell losses, as well as the the atomic physics details, are more severe. It has been customary to use an average atom (AA) to treat very high Z material. It offers the advantages of rapid calculation while at the same time some treatment of complex L- and M-shell electronic structure. However, because various rates are scaled from hydrogenic formulas it also may overemphasize the effect of radiative transitions. Thus the poor yield from xenon in Table III may be indicative of the difficulty in achieving the K-shell ionization stage due to the dominant L- and M-shell energy sinks, or it may be only a reflection of the inherent assumptions of the AA approach.

(iv) Closely connected to the ionization dynamics of high Z materials is the radiation transport of the free-bound continuum emission. In the J-scaling law of Ref.3, the total K-shell emission is included in yield estimates. For the present work, ZPIMP uses a probability-of-escape technique for the free-bound emission which transports all the emitted radiation as if it had the frequency at the edge. In order to increase the yield in the highest energy (> 30 keV) bins, load composition and design may be engineered to put out most of the high energy radiation from recombination to K-shell states. In this case a *multi-frequency radiation transport* is the technique for properly calculating the emitted spectrum. Since the He- and H-like continuum for krypton and xenon extends far beyond the edge, the opacity evaluated at the edge is inaccurate. In the high energy photon bins the shape of the spectrum is important for determining what is essentially a small component of the total emitted radiation. One should also note that by the nature of an AA atomic physics model, the free-bound continuum from the K-shell stages is underestimated whenever the mean charge state $\langle Z \rangle$ is less than $Z_{nuc} - 2$. Because the bound energy levels in a AA model are not as negative with a higher $\langle Z \rangle$, the free-bound continuum is shifted to lower energies

than it should be for $\eta \sim 1$ implosions wherein the bulk of the plasma is not in the K-shell. Thus a realistic estimate of the highest energy emission is best accomplished with a DCA atomic model [point (iii) above] in conjunction with multi-frequency radiation transport. The drastic conclusion that a PRS cannot produce the required high energy (> 30 keV) radiation yield and one must look to other techniques, is at the least simply premature. Future work on the high energy component could address the problem of xenon ionization dynamics with a modified DCA atomic model and multi-frequency transport.

(v) Finally, the present ZPIMP code is designed to run off of a lumped circuit model for the circuit. This is acceptable for the linear voltage adder for which the voltage pulse originates far away in time from the load and the load behavior does not alter the pulse, except for long $\gtrsim 200$ nsec implosion times. But for any inductive storage design, the driving open circuit voltage is effectively that created across the plasma opening switch. This element is close to the load and the voltage does respond to the load's behavior. The scaling law calculations of Ref.3 do treat the circuit as a transmission line, but ZPIMP, and more advanced multi-zone 1-D and 2-D codes, should be revised to do likewise. This would allow detailed simulation models to address specific aspects of power flow and load coupling on various machine designs, particularly if the revised code also included electron losses in magnetically insulated transmission lines. The extra difficulty in self-consistently coupling the energy from a transmission line circuit into the front end load region lies in the diffusion of the external magnetic field inside the plasma region. This problem is presently under development. The revised ZPIMP code should also investigate radiation yields from the recent JUPITER design versions for the LIA and IES. Both deliver more kinetic energy than the circuit used in the present paper and offer the potential for larger yields than LIA-1 in the energy bins of Table III. In these new designs Ref.3 showed that improved K-shell yields for argon could be achieved if the pinch length was increased from 4 to 6 cm, while shorter pincher lengths (~ 2 cm) proved beneficial for xenon.

Acknowledgments

This research was supported by the Defense Nuclear Agency under contract number 67-5493-0-4 94. J. Giuliani would like to thank Ken Whitney of the Radiation Hydrodynamics Branch for providing the SATURN data and many other members of the JDOST with which he had fruitful discussions, especially Pat Corcoran of Pulse Sciences Inc. for assistance in calculating an open circuit voltage, Bob Commisso of the Naval Research Laboratory for emphasizing the requirements/capabilities matrix, and Nino Pereira of Berkeley Research Associates for pointing out the angle correction to the yield at the target edge.

References

- [1.] K.G. Whitney, J.W. Thornhill, J.L. Giuliani Jr., J. Davis, L. Miles, G. Nolting, V. Kenyon, W. Speicer, R.B. Spielman, T.J. Nash, J.S. McGurn, L.E. Ruggles, C. Deeney, R.R. Prasad, and L. Warren, "Optimization of K-Shell Emission in Aluminum Z-Pinch Implosions: Theory versus Experiment," submitted to *Phys. Rev. E*, February (1994).
- [2.] J. L. Giuliani, Jr., M. Mul Brandon, J. Davis, P. Ottinger, R. Commisso, C. Deeney, and P. D. LePell, "Numerical Simulations of PRS Yields for a Pulsed Power DECADE-Class Generator," accepted for publication *J. of Radiation Effects, Research and Engineering*, (1994).
- [3.] J. L. Giuliani, Jr., J. Davis, M. Mul Brandon, K. Whitney, and J. W. Thornhill, "PRS Scoping Study I: Scaling Law Estimates for K-Shell Radiation Yields on JUPITER-Class Generators," previous paper in load group section of the JDOST report. Submitted as a *Naval Research Laboratory Memorandum Report*, (1994).
- [4.] K.G. Whitney, J.W. Thornhill, J.P. Apruzese, and J. Davis, "Basic Considerations for Scaling Z-Pinch X-Ray Emission with Atomic Number," *J. Applied Physics*, 67, 1725 (1990).
- [5.] J. W. Thornhill, K. G. Whitney, C. Deeney, and P. D. LePell, "Phenomenological Modeling of Turbulence in Z-Pinch Implosions," *Phys. Plasmas*, 1, 321 (1994).
- [6.] J. L. Giuliani, Jr. and J. Rogerson, "ZPIMP: A Zero-D Z-Pinch Implosion Code," *Naval Research Laboratory Memorandum Report*, 6448, (1989).
- [7.] W.D. Schulz, "Two-Dimensional Lagrangian Hydrodynamic Difference Equations," *Methods in Computational Physics*, Vol.3, (Ed. B. Alder, S. Fernbach, and A. Rotenberg, Academic Press: New York 1964), p.1.
- [8.] S. I. Braginskii, "Transport Processes in a Plasma," *Reviews of Plasma Physics*, Vol. 1, (Ed. M. A. Leontovich, Consultants Bureau: New York 1965), p.205.
- [9.] I. K. Aivazov, V. D. Vikharev, G. S. Volkov, L. B. Nikandrov, V. P. Smirnov, and V. Ya. Tsarfin, "Formation of Axial Fore-plasma Channel in the Initial Stage of the Compression of a Multi-wire System by Megampere Currents (Experimental)," *Soviet J. Plasma Phys.*, 14, 110 (1988)
- [10.] C. Deeney, P. D. LePell, B. Failor, J. Meachum, S. Wong, J. W. Thornhill, K. G. Whitney, and M. C. Coulter, "Radius and Current Scaling of Argon K-Shell Radiation," accepted for publication *J. Applied Physics*, (1993).

- [11.] D. Duston, R. W. Clark, J. Davis, and J. P. Apruzese, "Radiation Energetics of a Laser-Produced Plasma," *Phys. Rev. A*, 27, 1441 (1983).
- [12.] F. Perrot, "Fast Computation of Electronic Structure in Plasmas, The Screened Hydrogenic Model with L-Splitting," *Journal de Physique, Colloque C7, Supplement au n°12, Tome, 49*, (Dec., 1988).
- [13.] F. Perrot, "Fast Calculation of Electronic Structure in Plasmas, The Screened Hydrogenic Model with L-Splitting," *Physica Scripta*, 39, 332, (1989).
- [14.] R. M. More, "Electronic Energy Levels in Dense Plasmas," *J. Quant. Spect. Rad. Transf.* 27, 345 (1982).
- [15.] R. Marchand, S. Caille, and Y. T. Lee, "Improved Screening Coefficients for the Hydrogenic Ion Model," *J. Quant. Spect. Rad. Transf.* 43, 149 (1990).
- [16.] D. E. Post, R. V. Jensen, C. B. Tarter, W. H. Grasberger, and W. A. Lokke, "Steady-State Radiative Cooling Rates for Low-Density, High-Temperature Plasmas," *Atomic Data and Nuclear Tables*, 20, 397 (1977).
- [17.] J. P. Apruzese, "Direct Solution of the Equation of Transfer Using Frequency- and Angle-Averaged Photon-Escape Probabilities for Spherical and Cylindrical Geometries," *J. Quant. Spect. Rad. Transf.* 25, 419 (1981).
- [18.] J. P. Apruzese, "An Analytic Voigt Profile Escape Probability Approximation," *J. Quant. Spect. Rad. Transf.* 34, 447 (1985).
- [19.] R. Spielman, private communication (1990).
- [20.] I. Smith, "Inductive Adder Designs for Jupiter," presentation at 1'st JDOST meeting, Albuquerque, NM, July (1993)
- [21.] K. G. Whitney, J. Davis, and J. P. Apruzese, "Influence of Broadband Photocoupling on K-Shell Excitation in Aluminum," *Phys. Rev. A*, 22, 2196 (1980).
- [22.] J. P. Apruzese, private communication.
- [23.] T. Kennedy, "Joint DoD/DOE Minimum Jupiter Goals," presentation at 3'rd JDOST meeting, Albuquerque, NM, October (1993)
- [24.] M. Hedermann, see Testing Technologies Section of the final JDOST Report, Sandia National Labs, (1994).

- [25.] H. W. Bloomberg, M. Lampe, and D. G. Colombant, "Early Expansion in Exploding Multiple Wire Arrays," *J. Applied Phys.*, **51**, 5277 (1980).
- [26.] K. G. Whitney, J. W. Thornhill, R. B. Spielman, T. J. Nash, J. S. McGurn, L. E. Ruggles, and M. C. Coulter, "Analysis of Recent SATURN Aluminum PRS Experiments," *Proceedings of the 3'rd International Conference on Dense Z-Pinches*, London, England: to be published (1994).
- [27.] T. Cochran and J. Davis, "Implosion Stability in 60 MA Z-Pinches," see Load Physics Section of the final JDOST Report, Sandia National Labs, (1994).
- [28.] J. Davis, "Comments on Load Physics Issues," presentation at the *2'nd JDOST Workshop*, Naval Research Lab., September (1993).